Annals of Glaciology

Article

Cite this article: Ackley SF et al. (2020). Sea-ice production and air/ice/ocean/biogeochemistry interactions in the Ross Sea during the PIPERS 2017 autumn field campaign. *Annals of Glaciology* **61**(82), 181–195. https://doi.org/10.1017/aog.2020.31

Received: 30 November 2019
Revised: 25 April 2020
Accepted: 27 April 2020
First published online: 11 June 2020

Key words:
Atmosphere/ice/ocean interactions; ice/ocean interactions; sea ice; sea-ice growth and decay

Author for correspondence:
S. F. Ackley,
E-mail: Stephen.ackley@utsa.edu

cambridge.org/aog

Sea-ice production and air/ice/ocean/biogeochemistry interactions in the Ross Sea during the PIPERS 2017 autumn field campaign

S. F. Ackley[1], S. Stammerjohn[2], T. Maksym[3], M. Smith[4], J. Cassano[5], P. Guest[6], J.-L. Tison[7], B. Delille[8], B. Loose[9], P. Sedwick[10], L. DePace[11], L. Roach[12] and J. Parno[13]

[1]Center for Advanced Measurements in Extreme Environments, University of Texas at San Antonio, San Antonio, TX 78249, USA; [2]Institute for Arctic and Alpine Research, University of Colorado, Boulder, CO, USA; [3]Department of Applied Ocean Physics and Engineering, Woods Hole Oceanographic Institution, Woods Hole, MA, USA; [4]Applied Physics Laboratory, University of Washington, Seattle, WA, USA; [5]Atmospheric and Oceanic Sciences, University of Colorado, Boulder, CO, USA; [6]Department of Meteorology, NPS, Monterey, CA, USA; [7]PROPICE Unit, Laboratoire de Glaciologie, Université Libre de Bruxelles, Bruxelles, Belgium; [8]Unité d'Océanographie Chimique, Astrophysics, Geophysics and Oceanography Department, University of Liège, Liège, Belgium; [9]Graduate School of Oceanography, University of Rhode Island, Narragansett, RI, USA; [10]Department of Ocean, Earth and Atmospheric Sciences, Old Dominion University, Norfolk, VA, USA; [11]Department of Science, US Coast Guard Academy, New London, CT, USA; [12]Atmospheric Sciences, University of Washington, Seattle, WA, USA and [13]Cold Regions Research and Engineering Laboratory, Hanover, NH, USA

Abstract

The Ross Sea is known for showing the greatest sea-ice increase, as observed globally, particularly from 1979 to 2015. However, corresponding changes in sea-ice thickness and production in the Ross Sea are not known, nor how these changes have impacted water masses, carbon fluxes, biogeochemical processes and availability of micronutrients. The PIPERS project sought to address these questions during an autumn ship campaign in 2017 and two spring airborne campaigns in 2016 and 2017. PIPERS used a multidisciplinary approach of manned and autonomous platforms to study the coupled air/ice/ocean/biogeochemical interactions during autumn and related those to spring conditions. Unexpectedly, the Ross Sea experienced record low sea ice in spring 2016 and autumn 2017. The delayed ice advance in 2017 contributed to (1) increased ice production and export in coastal polynyas, (2) thinner snow and ice cover in the central pack, (3) lower sea-ice Chl-*a* burdens and differences in sympagic communities, (4) sustained ocean heat flux delaying ice thickening and (5) a melting, anomalously southward ice edge persisting into winter. Despite these impacts, airborne observations in spring 2017 suggest that winter ice production over the continental shelf was likely not anomalous.

Introduction

From 1979 to 2015, the Ross Sea was the only place on Earth with large increases in sea-ice area, extent and annual duration (Fig. 1; Turner and others, 2009; Comiso and others, 2011; Parkinson and Cavalieri, 2012; Stammerjohn and others, 2012). A considerable amount of sea-ice production (SIP) in the Ross Sea takes place in two coastal polynyas – the large Ross Sea Polynya (RSP) and the smaller but intensely productive Terra Nova Bay polynya (TNBP) (e.g. Kwok, 2005; Drucker and others, 2011). Concurrent with the observed sea-ice extent increases in the Ross Sea, increases in wind-driven ice export from the Ross Sea coastal areas have been observed (Kwok, 2005; Haumann and others, 2016). Seasonally, the strongest sea-ice increases in the Ross Sea have been in autumn (e.g. Stammerjohn and others, 2012), when the ice pack is rapidly expanding due to enhanced ice growth, both within the polynyas and at the advancing ice-edge, along with net northward ice drift due to wind-driven advection (Haumann and others, 2016). How much each of these processes (i.e. SIP in polynyas, SIP at the ice edge, net northward advection) contribute to advancing and expanding the autumn ice cover in the Ross Sea is a key question, particularly for improving modeled simulations and identifying causes (Hobbs and others, 2016).

While an expanding sea-ice cover in the Ross Sea was the prevailing condition in the satellite era up until 2015, a sudden reversal took place starting in spring 2016, when November recorded a minimum extent, not just in the Ross Sea but also for Antarctic circumpolar-averaged sea-ice extent (e.g. Stuecker and others, 2017; Turner and Comiso, 2017; Turner and others, 2017; Schlosser and others, 2018). Lower-than-average sea-ice extent has continued in the Ross Sea since spring 2016, particularly in autumn, and has delayed the autumn ice-edge advance (e.g. Fig. 1). Neither the drivers of the sea ice increases over 1979–2015, nor for the unanticipated recent decreases, have been well established for the Ross Sea (e.g. Hobbs and others, 2016; Lecomte and others, 2017; Meehl and others, 2019; Purich and others, 2019).

As one of the most biologically productive areas in the Southern Ocean (Arrigo and others, 2008a; Smith and others, 2012) and a major source of deep-water formation (Gordon and others, 2004; Orsi and Wiederwohl, 2009), the Ross Sea continental shelf is thought to be

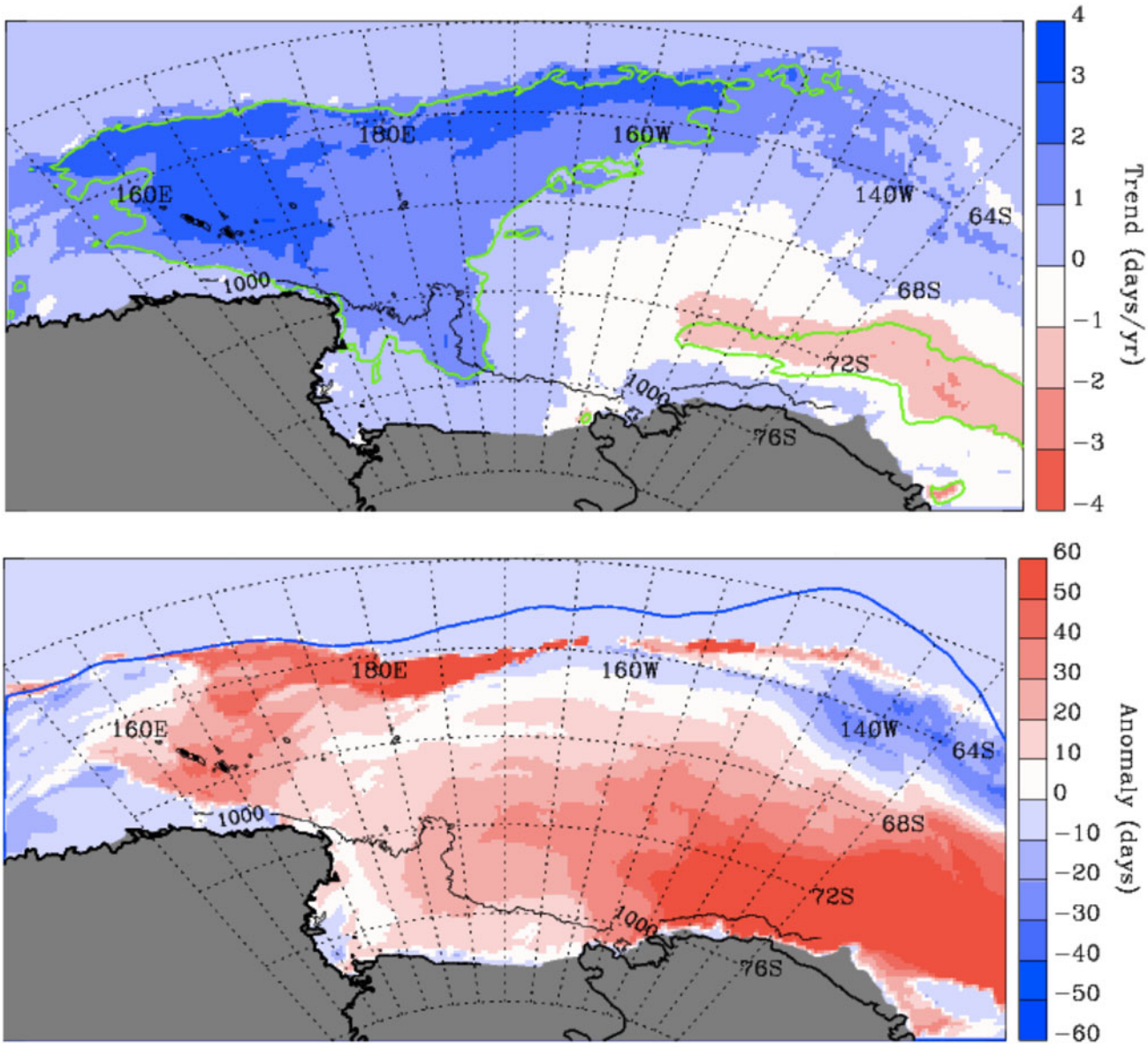

Fig. 1. (top) Trends (days yr^{-1}) in annual ice season duration over 1979–2015 (updated from Stammerjohn and others, 2012) showing strong positive trends (i.e. longer annual ice seasons) in the central-western Ross Sea, where ice season became ~2 months longer on average over 1979–2015. The green contour outlines those trends significant at the $p < 0.01$ level. (bottom) The 2017 anomaly (days) in the timing of the autumn ice-edge advance (compared to the 1980–2010 base period), showing a later ice-edge advance (red) across the Ross Sea and into the inner Amundsen Sea. The blue contour outlines the 1979–2018 climatological location of the September ice edge. The thin black contour in both images outlines the continental shelf-slope break.

an important regional sink for atmospheric CO_2 (Arrigo and others, 2008b; Tagliabue and Arrigo, 2016). Here, the magnitude of annual primary production is thought to be limited by the supply of dissolved iron (DFe) (Tagliabue and Arrigo, 2005). DFe is delivered to surface waters by melting sea ice and glacial ice, intrusion and upwelling of Circumpolar Deep Water, and the vertical resupply of iron-rich waters from the benthos (Sedwick and others, 2000; McGillicuddy and others, 2015). Vertical resupply is presumed to be most prevalent during the winter months when katabatic winds drive SIP and convective overturn in coastal polynyas (Marsay and others, 2014; McGillicuddy and others, 2015), although the impact of these processes on the water-column DFe distribution have not yet been established.

Changes in SIP and deep-water formation have further biogeochemical ramifications. Deep-water formation and net community productivity in the Southern Ocean are thought to be important to the solubility pump for anthropogenic carbon and other atmospheric gases. The solubility pump is most directly related to the rate of deep-water formation, and consequently, the strength of the carbon sink may change if the rate of deep-water formation changes (Nicholson and others, 2010; Meredith and others, 2011; de Lavergne and others, 2014). Given that the mechanism for deep water formation is closely tied to brine rejection by SIP, polynyas, as veritable 'ice factories' producing ~10% of the total modern Southern Ocean ice pack (Tamura and others, 2008), play a key role in the solubility pump and thus the strength of the carbon sink. However, the solubility pump for any gas also depends on water temperature (Hamme and Emerson, 2004), wind speed (Wanninkhof, 1992) and air bubbles in the surface ocean (Liang and others, 2013), necessitating simultaneous measurements of these parameters during active SIP (Loose and others, 2014) and deep-water formation.

The PIPERS project

The need to better understand processes driving SIP and the coupled air/ice/ocean/biogeochemical interactions in this region motivated the PIPERS program: *Polynyas and Ice Production*

and seasonal Evolution in the Ross Sea. The principal objectives of this program were to:

(1) Describe the regional atmospheric, ocean and ice conditions in the Ross Sea.
(2) Quantify SIP rates during the active autumn growth season, and assess the drivers (winds, waves, ocean/atmosphere thermal forcing).
(3) Understand the impact of changes in SIP on water mass transformation, particularly Shelf Water (SW) production.
(4) Improve understanding of coupled air/ice/ocean/biogeochemical interactions both regionally and in areas of high SIP (the ice edge and coastal polynyas).

Large uncertainties in SIP in the Ross Sea have global implications due to its association with the production of SW. SW is a precursor to the formation of Antarctic Bottom Water, which is a key driver of the global thermohaline circulation (Jacobs, 2004; Orsi and Wiederwohl, 2009). Large uncertainties in SIP are largely due to the fact that there are few in situ observations in the Ross Sea during autumn-winter. There have been three prior growth-season cruises in the Ross Sea – one each in autumn 1995 and 1998 (Jeffries and Adolphs, 1997; Tin and Jeffries, 2001), and one in winter 1995 (e.g. Adolphs, 1999). Both prior autumn cruises visited the RSP, while the 1998 cruise also visited TNBP (Jeffries and others, 2001a). These cruises observed autumn conditions that were fairly common for circumpolar Antarctic sea ice (Worby and others, 1998), characterized by a young first-year ice cover (~50–60 cm) and modest snow cover (~10–15 cm) (Jeffries and Adolphs, 1997; Tin and Jeffries, 2001). Thickening from autumn to winter in the outer pack ice as observed in 1995 was modest, in part because of retardation of basal growth due to ocean heat (Jeffries and others, 1998). Despite the modest snow depth observed in autumn, a significant percentage of snow-ice formation occurred, similar to other regions and seasons (Jeffries and others, 2001b).

Prior to PIPERS, there had not been a growth-season cruise in the Ross Sea since 1998 (19 years). Moreover, those previous autumn-winter field campaigns did not include a comprehensive approach to observing and measuring the coupled air/ice/ocean interactions driving SIP, its evolution over winter, and the dynamical processes affecting sea ice and snow distributions and thicknesses in spring. Such a comprehensive approach is also needed to improve our ability to determine sea ice and snow thickness from satellites, which is now more imperative given the recent launch of ICESat2. At present, errors in snow and ice thickness estimates from satellites are large (Kern and Spreen, 2015). A better understanding of the seasonal evolution of in situ coupled processes, particularly the distribution of snow on sea ice and its relationship to deformed and level ice, will lead to significant improvements.

To address these needs, the multi-national and multi-disciplinary PIPERS field campaign used a highly-coordinated combination of ship- and aircraft-based approaches and underwater, surface and air-borne autonomous platforms to measure the space-time evolution of air/ice/ocean/biogeochemical interactions and processes, initiated during autumn and tracked into winter-spring (Fig. 2; Table 1). Measurements were acquired within and outside the coastal polynyas and on/off the continental shelf, the latter both on the south- and northbound transects. Here, we provide a new cross-disciplinary analysis of the field data (expanded in space and time by satellite remote sensing) to highlight sea ice and ice/ocean/atmosphere/biogeochemical conditions leading up to, during and following the autumn 2017 field campaign, both in the coastal polynyas and across the wider Ross Sea region.

Approach and methods

The overarching approach was to create a synthesis of data from the following sources:

(1) Ship-based (in situ) observations of (i) the atmospheric and oceanic heat and momentum balance at the surface, simultaneous with observations of the atmospheric boundary layer and the effects of wind/wave interactions on sea-ice growth and thickness evolution; (ii) ocean property changes affecting ocean heat/salt budgets, sea-ice growth processes, and water mass distributions; and (iii) physical and biogeochemical properties of the sea-ice cover at representative locations (from the ice edge to the central pack to the coastal polynyas).
(2) A coordinated space-time buoy campaign using (i) wave buoys deployed in the outer pack ice to measure wind/wave/ice interactions during both the south- and northbound legs; (ii) deformational arrays of ice mass balance (IMB) buoys, GPS buoys and automated weather stations (AWS) deployed outside the polynyas in autumn to track air/ice/ocean interactions, ice thickness evolution/export, and pack ice divergence/convergence through the winter period; and (iii) an ocean mooring deployed in TNBP in early 2017 (and recovered in early 2018) to measure ocean/ice interactions and water mass transformation in response to katabatic wind events.
(3) Coordinated near real-time satellite retrievals to assist in cruise-planning and give space/time context for observations collected during PIPERS, as well as coordinated air campaigns in spring (November 2016 and 2017) to measure regional ice thickness.

Below, we describe the methods for acquiring these data during the PIPERS field campaign in autumn 2017 and during the spring air campaigns in November 2016 and 2017.

During the 2-month autumn 2017 field campaign, PIPERS sampled the open ocean bordering the Ross Sea and a variety of different ice conditions in the western-central Ross Sea (Fig. 3). Data acquired during the open ocean segments consisted of underway surface ocean, meteorological, and air-sea gas measurements. These included: radiative energy fluxes; surface air temperature; cloud ceiling height; sea-surface temperature (SST, measured by 3 IR guns, a 'sea snake' system and the ship's seawater intake); sea-surface salinity; fluorescence; pCO_2; methane and dissolved noble gases (N_2, O_2, Ar, and Ne collected with a membrane inlet mass spectrometer or UMS); and atmospheric gases (CO_2, CH_4, N_2O; discrete $^{14}CO_2$ and $^{14}CH_4$). Atmospheric profiles were obtained hourly to twice daily by radiosondes measuring temperature, humidity, pressure and winds to an altitude of 18 km. The approximate vertical resolutions for temperature, humidity and winds were 4, 15, and 50 m, respectively, with nominal accuracies of 0.2°C, 2%, and 2 m s^{-1}. These underway measurements were continued throughout the cruise. In addition, along the southbound open water track between 60°S and 68.5°S, three Argo floats and four SOCCOM floats were deployed, the latter alongside CTD rosette deployments (consisting of continuous vertical profiles of temperature, conductivity, dissolved oxygen, fluorescence, and beam transmittance, as well as discrete water samples for physical and biogeochemical parameters as listed in Table 2).

Once inside the ice edge, underway visual sea-ice observations were conducted hourly from the bridge using ASPeCt protocols (Worby and others, 2008) and included sea-ice type (Fig. 3), estimates of sea-ice thickness, ice concentration, and snow depth (see also Fig. 4). Sampling in the MIZ included wave buoy deployments, SWIFT drifters (Lagrangian surface floats that measure

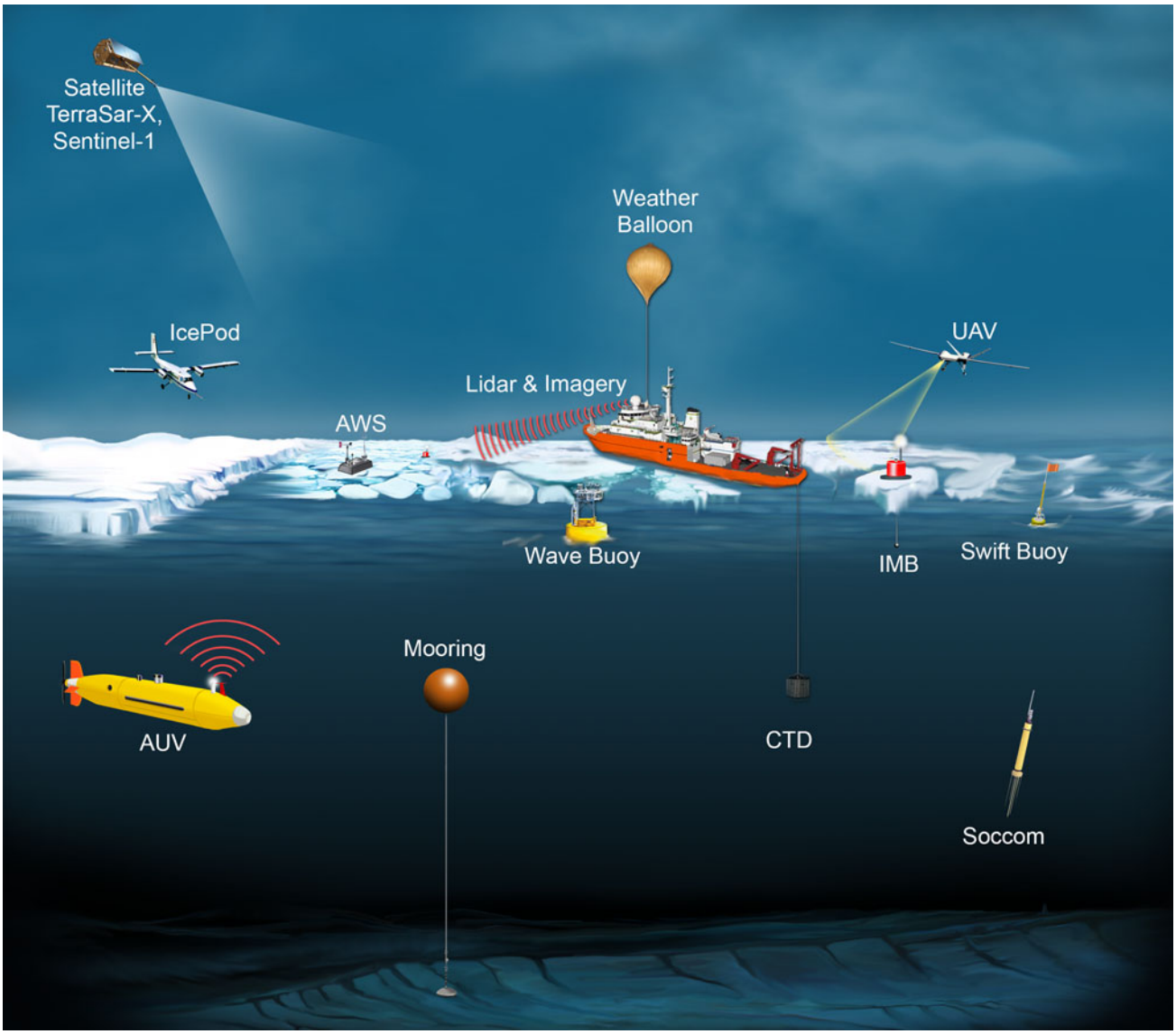

Fig. 2. Schematic of technologies used on PIPERS. Observational platforms included automatic weather stations (AWS), SWIFT and wave buoys, and ice mass balance (IMB) buoys, ship-based instrumentation (e.g. Conductivity-Temperature-Depth, CTD, rosette package), a mooring, an autonomous underwater vehicle (AUV), an unmanned airborne vehicle (UAV) and Southern Ocean Carbon and Climate Observations and Modeling (SOCCOM) floats. Not shown are the ice-based observations (i.e. ice stations) that are further described in the text.

surface waves, winds and other ocean and atmosphere properties; see Smith and Thomson, 2016), zodiac-based physical and biogeochemical sea-ice sampling, and ship-based CTD rosette deployments. Ice stations included both short (<1 day) and long (>1 day) stations (Fig. 3a, circles and squares, respectively), some of the latter also including Autonomous Underwater Vehicle (AUV) deployments (Fig. 3a, bowties). Short stations typically consisted of ice sampling, gas flux measurements and/or buoy deployments. Long stations typically consisted of a full suite of ice sampling and biogeochemical observations, spatial surface surveys of snow depth, surface topography and AUV ice thickness surveys, buoy deployments (with additional details given below), as well as atmospheric observations from flux towers, unmanned aircraft and radiosondes.

At each of the long ice stations, we conducted a comprehensive mapping of the snow depth, snow freeboard and ice thickness to examine how snow accumulates around deformation features and the relationship between surface topography and sea-ice thickness. At seven stations, a Seabed-class AUV mapped the ice thickness distribution with multibeam sonar over ~200 × 200 m area following Williams and others (2015) at sites selected to highlight deformation features (see Fig. 3a for locations). These were the first winter under-ice AUV missions in the Antarctic. Coincident surface surveys of snow depth and snow freeboard (i.e. the elevation of the snow/ice surface above sea level) were completed. The snow freeboard was mapped over a 100 m grid with a Riegl VZ-1000 terrestrial lidar scanner, and the snow depth was sampled at ~2000 points over the grid using a SnowHydro Magnaprobe, modified to provide improved location capabilities with post-processed kinematic GPS.

CTD vertical profiles were acquired throughout the cruise, yielding a cruise total of 58 profiles, and a trace-metal clean (TMC) CTD was also deployed in key areas (on the continental shelf along the southbound leg and in the polynyas), yielding a cruise total of 22 TMC CTD profiles. At each ice station, we acquired at least 1 CTD vertical profile, and between ice stations, CTD profiles were acquired at a spacing of ~0.5°–1° of latitude along the south- and northbound legs. In TNBP a higher concentration of both CTD and TMC CTD profiles were acquired along repeated zonal transits in/out of TNBP under varying katabatic wind forcing. Along the zonal transit of the RSP, both CTD and TMC CTD profiles were located at a spacing of 1°–2° of

Table 1. PIPERS sampling platforms, topics, investigators and measurements

Platform	Topic	Investigator(s)	Measurements
N.B. Palmer	Atmosphere	Guest, Cassano	Weather forecasting; ship/ice-based turbulent fluxes; boundary layer profiles (rawinsondes, UAV)
N.B. Palmer	Sea ice	Ackley, Weissling, Maksym, Delille, Tison	Ice cake sampling (texture, temperature, salinity, $\delta^{18}O$, Chl-*a*, CO_2, DMS); Shipboard digital photography; Underway Ice Thickness (EMI); Surface Elevation (Terrestrial Lidar); Snow Depth; AUV ice thickness
N.B. Palmer	Upper-ocean physics	Stammerjohn, Maksym, Smith	AUV and Ship CTD, T/S from IMBs, SWIFT buoys for turbulence and waves
N.B. Palmer	CO_2 Fluxes	Guest, Delille, Tison	Turbulent CO_2 fluxes; CTD profiling and Trace Metal water sampling; Underway pCO_2 and TCO_2; Floating Bell CO_2
NSF LC-130, Satellites	Sea ice	Xie, Ackley	Airborne Lidar Elevation and digital photography (LDEO IcePod System); Satellite Microwave
Autonomous Buoys	Sea ice and upper ocean	Maksym, Stammerjohn, Ackley, Guest, Kohout	Ice growth, drift and deformation; Ice Temperature Profiles; sea-water salinity and temperature (Ice Mass Balance Buoys and GPS Position Buoys); Meteorological spar buoy; WIIOS wave buoys
N.B. Palmer	Ocean	Sedwick	Iron and Trace Metals
N.B. Palmer	Ocean	Loose	Noble Gases: Underwater Mass Spectrometer, T/S and bottle sampling from ship CTD
TNBP Mooring	Ocean	Zappa, Gordon	Year-long mooring in near-shore Terra Nova Bay, measurements of T/S, upper ocean turbulence

N.B. Palmer is short for the RVIB *Nathaniel B. Palmer*.

longitude along the Ross Ice Shelf front. The UMS package was also deployed on the CTD at select stations in the polynyas, and water samples were collected to measure methane and dissolved noble gases (N_2, O_2, He, Ne, Ar, Kr, Xe). The dissolved noble gases shed light on the solubility pump and are used to distinguish the influence of deep-water formation processes, including SIP, water recharge temperature, and the amount of air injected as bubbles (Hamme and Emerson, 2004; Liang and others, 2013; Loose and others, 2014).

To track the dynamic and thermodynamic evolution of the ice cover as the winter progressed, four sea-ice buoy arrays were deployed (see Fig. 3a for locations). The first array consisted of three GPS position-only buoys deployed at the outflow of TNBP to measure the deformation of the outflow plume as it encountered the main Ross Sea pack. The other three arrays were deployed in the south central and western Ross Sea to monitor the ice evolution as it drifted northward from the RSP to the ice edge. Each of the latter three arrays consisted of 5-dice array patterns, spaced at 5–10 km intervals, with two ice mass-balance buoys (Jackson and others, 2013), one automatic weather station (temperature, humidity, pressure, wind speed and direction, and snow depth and ice thickness), and two GPS-only buoys.

Fourteen wave buoys (WIIOS: Waves-In-Ice Observation Systems) were deployed in the marginal ice zone (Kohout and others, in press, this issue). These buoys measure wave motions every 15 min using a high-precision inertial motion unit. Four of the WIIOS buoys were deployed in the MIZ on the transit south, and ten WIIOS buoys were deployed on the transit north over a span of ~200 nautical miles from the interior pack to the MIZ.

The biogeochemical component of PIPERS consisted of 27 sites along the cruise track where physical measurements were collected to support a suite of biogeochemical and ecological process studies focusing on major physical and environmental drivers (e.g. microbial production, nutrient recycling across the ocean/sea-ice/atmosphere interfaces, and gas exchange; see Tison and others, submitted, this issue). In addition to measurements at ice stations, zodiac-based measurements were acquired within the MIZ and coastal polynyas to capture biogeochemical processes during the first stages of sea-ice growth (i.e. unconsolidated ice, including frazil ice and thin pancakes). The data collected (Table 2) will also be used to validate and improve parameterizations of early winter sea-ice processes in climate and ecosystem models.

Coordinated near-real-time satellite image acquisition was critical for cruise planning, particularly in TNBP with its successive katabatic wind events. Terra-Sar-X quicklook imagery was sent to the ship, totaling 44 TDX images at ~15 m resolution. Also sent to the ship were Sentinel 1A and 1B images (totaling 50 images) at ~100 m resolution, as well as cloud-free MODIS images at 250 m resolution and daily maps of AMSR2 sea-ice concentration at 3.125 km resolution. Finally, SMMR-SSM/I imagery at 25 km resolution available from National Snow and Ice Data Center were used to place 2017 within the context of sea-ice variability and trends over 1979–2017 (e.g. Fig. 1).

Finally, there were two coordinated air campaigns in spring (November 2016 and 2017) to measure regional sea-ice thickness using the IcePod system flown onboard the NSF C-130 aircraft over the Ross Sea continental shelf in November 2016 and 2017. A particular emphasis was to repeat a flight line over a 'fluxgate' corresponding to the shelf-slope break to capture the export (rate) of pack ice from the continental shelf northward to the deep ocean (e.g. Kwok, 2005; Kwok and others, 2017). This area was also covered by NASA's IceBridge aircraft in 2013, allowing those data to be compared to ice thicknesses observed in 2016 and 2017 (Tian and others, submitted).

Results

Here we present an overview of observations made on (1) regional sea-ice conditions, (2) regional atmospheric conditions, (3) regional ocean conditions and (4) air/ice/ocean interactions in TNBP. More detailed analyses are published in companion papers (or are still pending); these are noted where relevant.

Regional sea-ice conditions

Underway observations of ice regimes and ice types

PIPERS sampled four different sea-ice regimes (Figs 3 and 4) as well as the open ocean bordering the marginal ice zone. These regions were characterized as follows (with dates of occupation included in parentheses):

(1) Open ocean, including both the inbound track (11–19 April) and the outbound track (5–12 June). The ocean north of the advancing ice edge, when crossed during both the inbound and outbound tracks, was characterized by anomalously warm waters and periodically high wind/wave conditions.
(2) Marginal Ice Zone (MIZ), including both the inbound track (19–22 April) and the outbound track (3–5 June). The autumn ice edge on the inbound track was anomalously

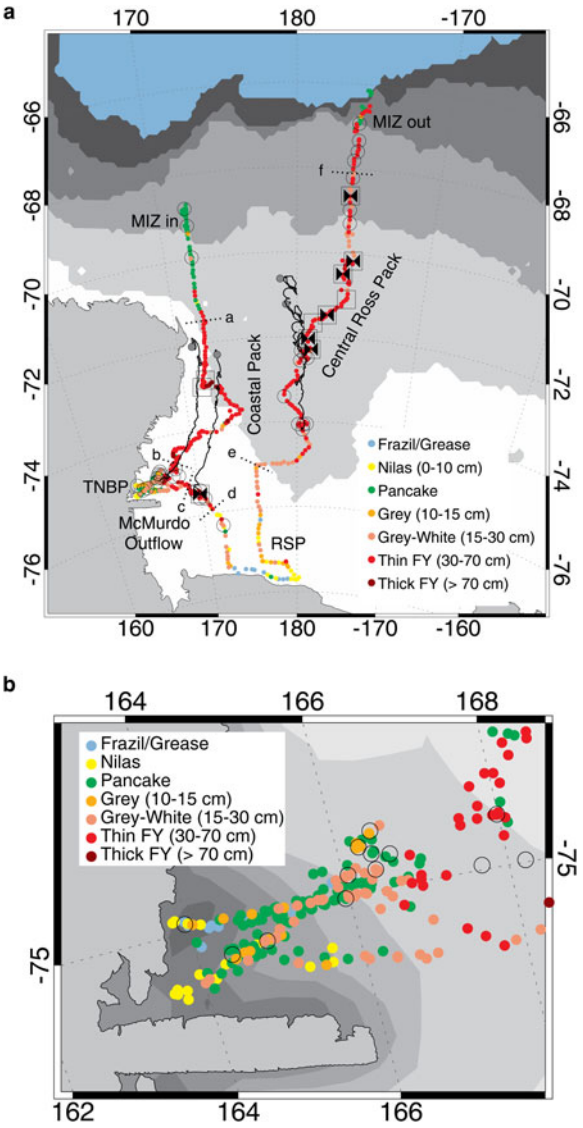

Fig. 3. (left) PIPERS cruise track within the sea ice zone, color-coded by observed ice type. The open circles are short (<1 day) stations; open squares are several-day ice stations; bow-ties are AUV stations. Buoy drifts (black lines) for one buoy from each buoy array from date of deployment to Jun 30 are also shown. Dotted black lines bisecting the cruise track roughly delineate ice regimes described in the text. Dates on which the ship crosses these delineations are (a) 23 April, (b) 30 April, (c) 12 May, (d) 15 May, (e) 19 May, (f) 3 June. The background white-gray shading corresponds to Advanced Microwave Scanning Radiometer 2 (AMSR2) ice extents for 1 April, 15 April, 1 May, 15 May, 1 June (defined with a 15% concentration cutoff). MIZ is marginal ice zone, TNBP is Terra Nova Bay polynya, RSP is Ross Sea Polynya. Note, only the cruise track at/inside the ice edge is shown here (and does not include the open ocean portions from/to Lyttleton, NZ). (right) PIPERS cruise track in TNBP (30 April—12 May), color-coded by observed ice type. The gray-shading corresponds to AMSR2 ice concentration on 1 May, with gray shading indicating ice concentration from 40% (darkest grey) to 90% (lightest grey).

south of its mean location and characterized by a wide (~200 km) zone of mostly pancake ice and a moderate-to-high sea state (with significant wave heights ranging from 1 to 4 m). The MIZ observed during the outbound transit was characterized by a relatively narrow MIZ, still south of its mean location, actively melting, consisting mostly of young first-year sea ice and a relatively high sea state.

(3) First-year ice, including thin (30–70 cm) and thick (>70 cm) rafted/ridged first-year ice. The young first-year ice cover of the coastal pack along Victoria Land (23–30 April) along the southbound leg became increasingly rafted and under pressure as TNBP was approached. Some of the thickest first-year ice observed was along the Victoria Land coast (Fig. 3), an area subject to heavy deformation against the coast. Along the northbound leg, the central outer pack ice north of RSP (19 May—2 June) was characterized by thin first-year ice and a long period swell. Thick first-year (>70 cm) ice was occasionally observed along the northbound leg in isolated ridged areas of the central Ross Sea.

(4) Coastal polynyas, including newly formed ice (<30 cm) in both the TNBP (30 April—12 May) and RSP (16–17 May). During our occupation of the TNBP, there were consecutive katabatic wind/wave events conducive to rapid pancake ice formation. In the RSP, there were moderate off-ice winds conducive to nilas (0–10 cm) and young grey ice (10–15 cm) formation.

(5) Wind-driven outflows from the coastal polynyas, including a range of deformed and undeformed young ice types. In the outflows from McMurdo Sound polynya and TNBP, the ice cover was heavily rafted (and often thick). The outflow from TNBP, in particular, may be one of the few locations in Antarctica where 'Dragon Skin Ice' can be observed (Fig. 5). In contrast, the ice in the northward outflow from the RSP (17–19 May) generally increased in thickness from frazil and nilas in the polynya proper to broad expanses of undeformed young grey and grey-white ice (15–30 cm).

Table 2. The suite of measurements collected as part of the biogeochemical component

Topic	Measurements
Physics and inorganic chemistry	Temperature
	Bulk salinity
	Water stable isotopes
	Ice fabrics
Gases	Bulk concentration of N_2, O_2, Ar, CH_4, N_20
	CO_2, DMS, DMSP, DMSO, VOC
	^{13}C and ^{2}H isotopic composition of CH_4 and ^{15}N and ^{18}O isotopic composition of N_2O
	Total gas content
	Measurement of air-ice-ocean fluxes of CO_2, CH_4, N_2O and VOC
Biology	Chl-*a* (fluorescence) and other pigments (HPLC) for different size class of microalgae
	Targeted enumeration of algal species
Biogeochemistry	Nutrients
	POC
	DOC
	$\delta^{15}N$
	Major elements (Cl, I, Br, …)
Trace Metals	Fe, Zn, Mn, Cu, Cd, Ni, V, Mo, Co, Ba, Al, Ga, Pb, REE
Carbonate System	Total Alkalinity (TA)
	pH
	$CaCO_3$ crystals (Ikaïte) derived from TA anomaly

Underway and station-based sea-ice thickness measurements

Overall, a relatively thin ice cover was observed throughout the central Ross Sea region with modal values for level (undeformed) sea ice typically <0.40 m with snow cover <0.10 m (Fig. 4). These values are generally lower than the sea ice and snow thickness values observed during two previous May–June cruises in the Ross Sea (in 1995 and 1998; Jeffries and Adolphs, 1997; Tin and Jeffries, 2001), and partially reflect the shorter ice growth season in 2017 relative to other years (Fig. 1). However, this may also reflect differences in ice types encountered along different cruise tracks. In the autumn of 2017, the thinnest and youngest ice observed was in the TNBP and RSP, mostly consisting of pancake ice and nilas ice, respectively. The prevalence of nilas in RSP reflects the generally lower wind conditions during our short occupation. The outflow from the RSP was also much thinner

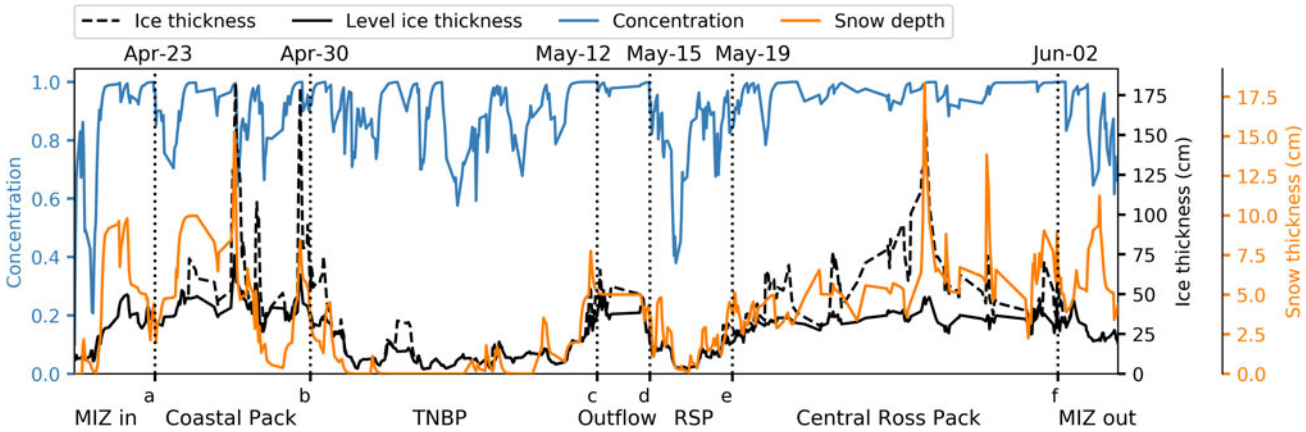

Fig. 4. Underway ice concentration (left *y*-axis; blue), ice thickness (inside right *y*-axis; black) and snow depth (outside right *y*-axis; orange) from hourly visual ice observations. The dashed black line is the ice thickness accounting for ridging, and the solid black line is the level ice thickness. The vertical dotted lines, lettered a-f, correspond to the delineations highlighted in Figure 3a. On the basis of comparisons with drilled measurements the error associated with thin ice such as nilas and grey-white ice <10 cm thick is ± 50%; for ice between 0.1 and 0.3 m the error is ± 30%; and for level ice >30 cm the error is ± 20% (Worby and others, 2008).

Fig. 5. The N.B. Palmer alongside rafted pancake ice (known as 'dragon skin') in the TNBP outflow. Pancakes are ~0.5–1 m in diameter and were vertically rafted in places, resulting from strong wind-driven advection out of TNBP to subsequently pile up against the northward drifting, often heavy pack ice. The orange and white measuring stick (pointing left over the pancake field from ship's starboard) has delineations of 5 cm and was used to estimate floe size and thickness (of upturned floes) from the starboard wing of the bridge. The visible 'shear line' stretching diagonally across the pancake field reveals the active deformation that was occurring at this site. (Photo by S. Stammerjohn).

and less rafted compared to previous observations (and compared to the outflow from TNBP, as noted above).

In contrast to these 2017 observations, the only other winter observations from 1995 saw much less open water in the TNBP and much thicker and ridged ice at the TNBP outflow (Jeffries and others, 2001a). Likewise, the outflow of thin ice from RSP was narrower in 1995, with thicker ice observed ~200 km north of the Ross ice shelf (Jeffries and Adolphs, 1997). In 2017, thin,

very level ice persisted for almost 400 km from the Ross ice shelf. These observations suggest that the TNBP and RSP were much more active in 2017 (Dai and others, 2020), with generally more divergent conditions in the central pack ice. Consequently, sea-ice export was likely greater than in prior observations, facilitated in part by the later development of the ice cover, thus a thinner less consolidated pack ice that allowed increased transport of ice northward. Additionally, there was more active local forcing in TNBP (see below). Despite these differences in the polynyas and central pack ice observed in 1995 vs 2017, sea-ice thicknesses in the outer Ross Sea in 2017 were similar to those observed in prior years (e.g. Jeffries and Adolphs, 1997). Tison and others (submitted, this issue) provide additional details on sea-ice structural differences encountered in 1998 vs 2017.

Station-based sea-ice biogeochemistry

Tison and others (submitted, this issue) demonstrate how the peculiar sea-ice growth conditions in 2017 led to considerably lower Chl-*a* burdens compared to both the previous early winter cruises in the Ross Sea (1995, 1998) and to other early winter cruises elsewhere in the Antarctic (Tison and others, 2017). A change in the sympagic community structure towards *Phaeocystis*-dominated cell abundances was also observed in 2017 (instead of diatom-dominated assemblages as noted in earlier reports of, e.g. Garrison and others, 2005). The 'health status' of this sympagic community, inferred from the Phaeopigments to Chl-*a* ratios, suggested active growth (relatively low proportion of dead cells vs active cells), but less than that observed for the Weddell Sea (Tison and others, 2017). Finally, the active primary production inferred from a March 2017 satellite image of TNBP was not apparent in our TNBP biogeochemical samples that were later collected in early May 2017. However, the inferred active primary production observed in March 2017 in TNBP may have seeded some of the algal stocks observed in our biogeochemical ice samples acquired further north along Victoria Land. Tison and others (submitted, this issue) provide additional details on sea-ice structure and the physical and biological properties of the sea ice. Much of the biogeochemical data are still being processed and interpreted, with results forthcoming.

Station-based sea-ice morphology and snow depth distribution

Surveys from the AUV, terrestrial lidar scanner, and snow magnaprobe were co-registered and compiled to provide coincident, high-resolution topography of the snow, ice surface and ice underside at four stations (e.g. Fig. 6). The AUV data revealed that very thick ridging can occur despite the young, thin ice cover, with the surveyed ridges all having keel depths greater than what is typically found in drilling surveys (Tin and Jeffries, 2003). Additional details and analysis are given in Mei and others (2019).

Buoy-based wave/ice interactions, sea-ice drift, and thickness evolution

The WIIOS (wave) buoy arrays indicated that waves from the Southern Ocean were a prominent and persistent feature in the outer pack north of the IMB arrays. The observed waves attenuated exponentially as they propagated into the pack ice, with attenuation rates dependent on sea-ice fraction. Additional analyses and greater details are given by Kohout and others (in press, this issue).

Due to the episodic high wind and wave conditions at the ice edge causing convergence/divergence in the outer pack ice, together with an overall thin first-year ice cover, the attrition rate for the drifting IMB buoys was high, with few mass-balance observations lasting more than a few weeks. However, a few buoys did last into November 2017. Surviving IMBs showed only modest ice growth as winter progressed, suggesting high ocean heat flux driven by remnant heat in the mixed layer and/or entrainment of heat from the pycnocline as the mixed layer continued to deepen. The high IMB attrition after only a few weeks from deployment highlights the highly dynamic conditions that led to significant new ice production in the outer pack ice. Due to the late onset of freeze-up in 2017, the amount of deformation observed during PIPERS was low compared to prior winter cruises (Tin and Jeffries, 2003), but as winter progressed, increased deformation contributed to the dynamical (vs thermodynamical) thickening of the pack ice.

Aircraft-based spring sea-ice thickness observations

Icepod aircraft surveys showed differences in regional sea-ice thickness in spring 2016 and 2017 compared to prior spring observations (Tian and others, submitted). Measurements were compared to IceBridge observations in 2013 and to ICESat data from 2003 to 2008. In general, the observations all show that new sea ice produced in the coastal polynyas (e.g. TNBP and RSP) is transported northward and thickens as it travels north. Interestingly, thicker sea ice was observed in spring 2017, compared to 2013 and 2016, suggesting that the delayed ice advance in 2017 drove only a temporary decrease in ice volume, and other processes (such as deformation and winter precipitation variability) likely compensated during winter. Compared to the IceSAT period (2003–08), sea-ice thickness along the coast from TNBP northward was greater in both 2016 and 2017, while sea-ice thickness offshore of the RSP and along the flux-gate was thinner compared to 2003–08 (Tian and others, submitted).

Regional atmospheric conditions

Continuous underway measurements of air temperature (measured at 9 m) along the PIPERS cruise track ranged from near-freezing temperatures over open water to as low as −29°C near the continent during katabatic wind events. As is typical for sea-ice regions, the relative humidity near the surface over ice-covered areas of the Ross Sea remained close to the ice saturation value. Well-mixed atmospheric boundary layers existed everywhere, ranging in depth from 150 m near the continent to 2500 m over open water. The extreme high winds, cold temperatures and open water in the Ross Sea coastal polynyas created turbulent heat fluxes of over 2500 W m^{-2}, among the largest observed on Earth, and capable of producing ice at rates of up to 0.70 m day^{-1} (with more details given below). Where there was substantial older ice and snow cover, the surface heat flux was dominated by the net longwave radiation, which in turn was controlled by cloud cover. Total longwave radiation ranged from ~20 W m^{-2} (upward) during overcast condition (60% occurrence) to 100 W m^{-2} during clear skies (20% occurrence).

Regional ocean conditions

Water mass distributions

The main water masses observed during PIPERS were, from surface to deep: Antarctic Surface Waters (AASW, <28 kg m^{-3}), Circumpolar Deep Water (CDW, 28.0–28.27 kg m^{-3}), sea ice-produced Shelf Water (SW, >28.27 kg m^{-3}, <−1.85°C) and Ice Shelf Water (ISW, >28.27 kg m^{-3}, <−1.95°C), defined using water masses as described in Orsi and Wiederwohl (2009). Shelf water can be separated into High Salinity Shelf Water (HSSW, salinity >34.62), found mostly in the western Ross Sea, and Low Salinity Shelf Water (LSSW, salinity <34.62), found mostly in the eastern Ross Sea (east of the RSP). The difference in salinity is reflective of differences in SIP, as greater SIP results in saltier SW. On the continental shelf, CDW was slightly lighter (closer to 28 kg m^{-3}) compared to its density off the shelf (closer to

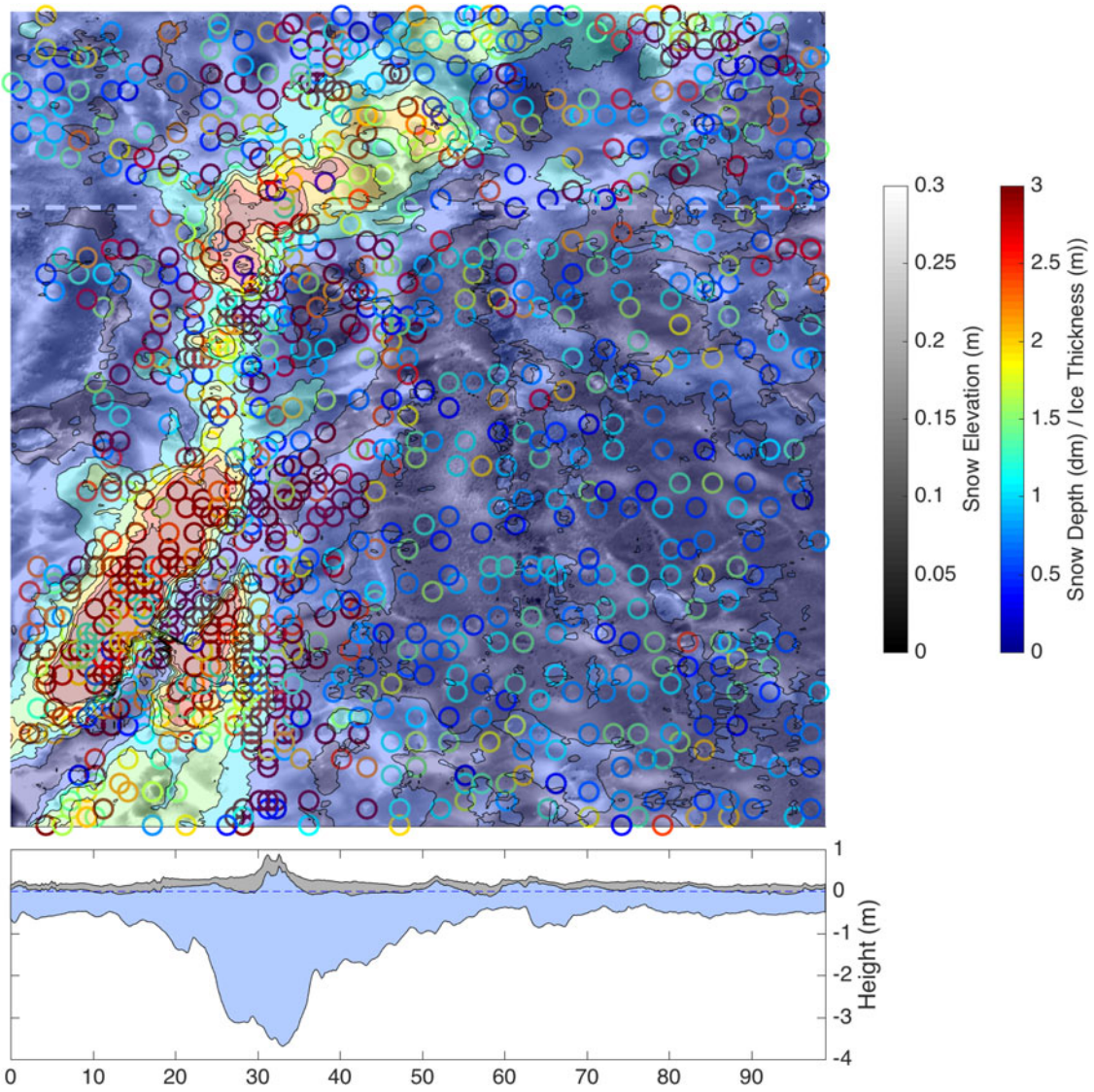

Fig. 6. Coincident, high-resolution topography of the snow, ice surface, and ice underside in planar view (top) for a 100 m × 100 m survey, and in vertical view (bottom) for the dashed transect (shown in top view). In the planar view, the underlying light/dark shading provides the surface topography from Lidar (inside right gray-shaded color bar) and the filled color contours are the AUV ice thickness (far right color bar, ice thickness in meters), while the colored circles are the snow depth (far right color bar, snow depth in decimeters).

28.27 kg m^{-3}) and is referred to here as modified CDW (mCDW). An example of a latitude-depth section of CTD data acquired along the southbound leg into TNBP shows the autumn distribution of AASW, mCDW and SW in salinity/density space compared to their climatological distribution in summer (Fig. 7). Isolated pockets of ISW were also detected in the TNBP (not resolved in Fig. 7), as well as in front of the Ross Ice Shelf.

Compared to the summer composite data, the bottom layer of SW was thinner and less salty during PIPERS in autumn 2017, most likely reflecting the slow start of SIP in driving deep convective overturning. (By end of winter, the net effect of SIP should generally produce a thicker, saltier layer of SW, with temperature and salinity characteristics similar to the SW in the summer composite.) Nonetheless, during strong katabatic wind events in TNBP (>30 m s^{-1}), deep convective mixing was observed, deepening the mixed layer from ~200 to 600 m over lateral distances of <10 km. In contrast, an overall shallower mixed layer in the RSP was observed (not shown), indicating that deep convective mixing was lagging compared to TNBP. It is also noted that the layer of CDW north of the shelf is slightly thicker (higher in the water column) than in the summer composite (and its temperature higher; not shown). Preliminary investigations also indicate that TNBP bottom waters observed during PIPERS were fresher compared to long-term TNBP mooring observations (Russo and others, 2011), and are suggestive of a freshening rate of ~0.02 decade^{-1}. Jacobs and Giulivi (2010) similarly reported a SW freshening rate of 0.03 decade^{-1} over 1958 to 2008 for the southwestern Ross Sea. However, our estimated freshening rate of TNBP SW may have an early season bias if SW production was not yet fully underway; a more rigorous assessment using oxygen isotope and noble gas measurements acquired during PIPERS is planned, and may help resolve any bias.

Dissolved iron distribution

Hydrographic data and water-column samples for analysis of iron and other trace metals were collected along the PIPERS cruise track, with particular focus on the polynyas. In response to the intense katabatic wind events observed in TNBP, the DFe data suggest that vertical mixing was starting to excavate the dense, iron-enriched HSSW that fills the deeper TNBP basin (Fig. 8, top), providing a potential source of DFe to the upper water column in the western Ross Sea. There is also evidence of lateral DFe inputs in the upper 500 m of the water column in TNBP. Stations in the RSP (in front of the Ross Ice Shelf), where wind conditions

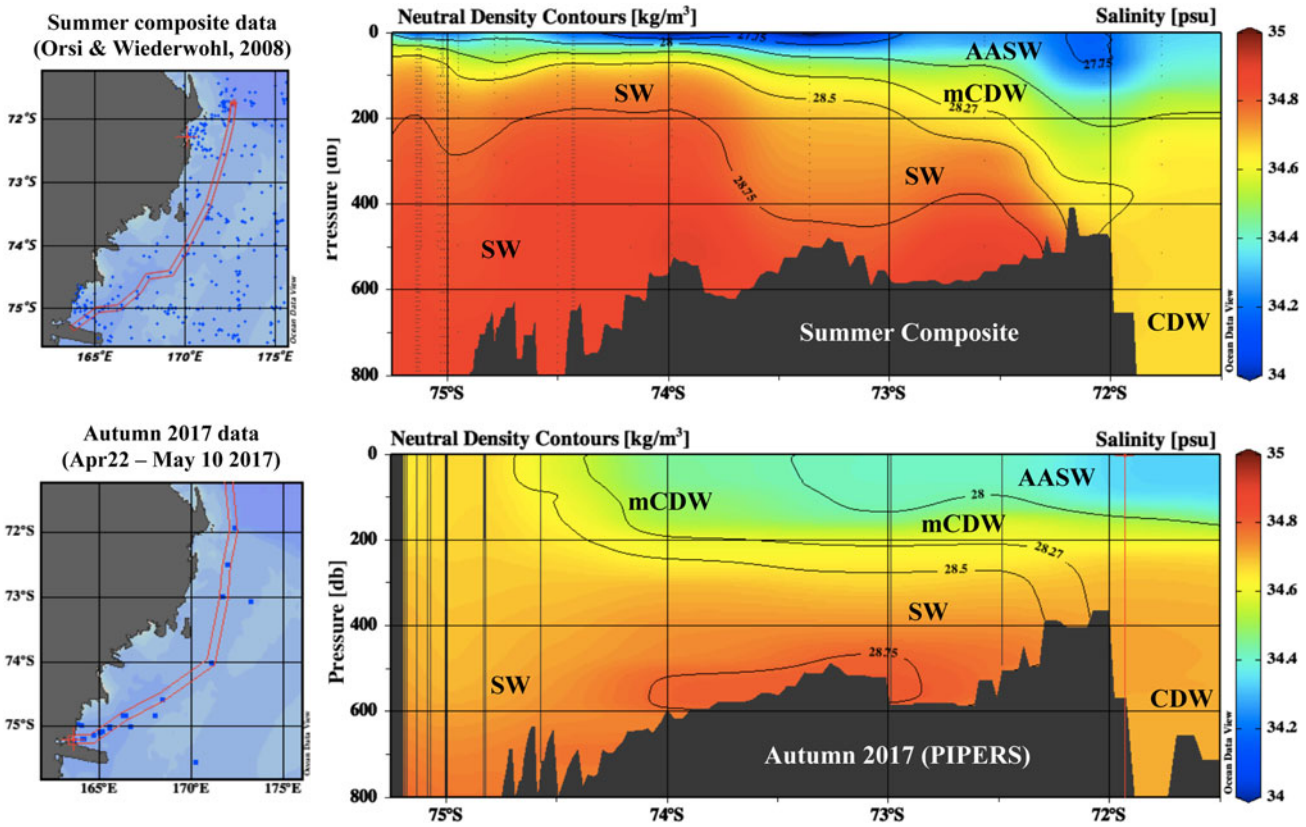

Fig. 7. Latitude-depth sections of salinity (color shading) and neutral density (black contours) in the western Ross Sea from just north of the continental shelf break to TNBP for: (top) a summer composite (see Orsi and Wiederwohl, 2009), and (bottom) autumn 2017 (as acquired by PIPERS between 22 April and 10 May). Water masses are defined in the text.

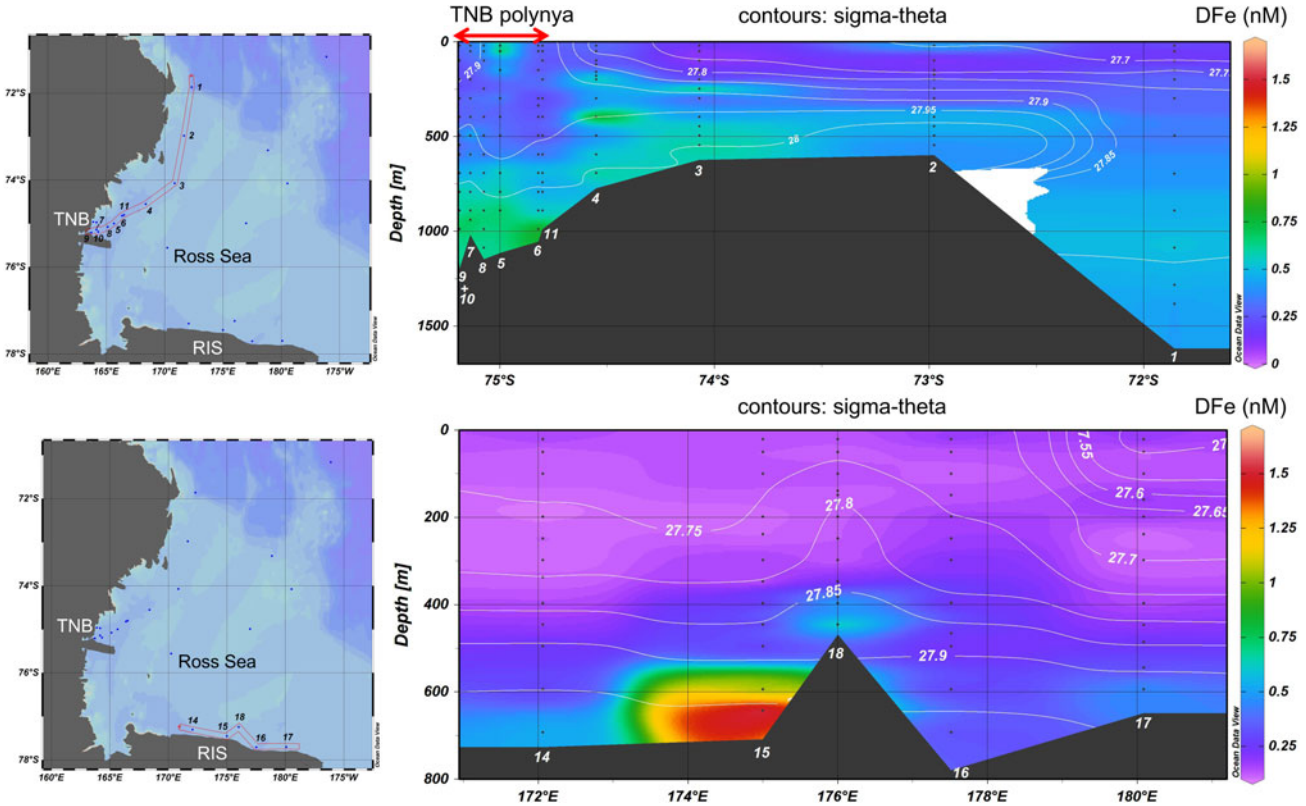

Fig. 8. Latitude-depth (top) and longitude-depth (bottom) sections of dissolved iron (DFe) concentration (color shading) and density (sigma-theta, kg m^{-3}, white contours) from just north of the continental shelf break to TNBP (top) and along the Ross Ice Shelf (bottom). The white numbers at the bottom of the sections correspond to profile numbers in the maps on the left.

were less extreme, revealed surface mixed layers <300 m depth, and a DFe distribution (Fig. 8, bottom) similar to previous, late-summer observations. Together, these results suggest that convective mixing progresses slowly during the winter months, with an earlier onset in the TNBP relative to the RSP, consistent with the observed timing of ice edge advance in these two polynyas during the cruise period (Fig. 1). Additional observations from the winter season are needed to fully elucidate the seasonal dynamics of DFe on the Ross Sea continental shelf.

Dissolved gases

A first look at the dissolved gas properties during late autumn in TNBP and RSP reveals strong modification of water properties as a result of convection, with noble gas concentrations far away from equilibrium with the atmosphere. Despite the extreme cooling and strong convection, the fingerprint of sea-ice formation was observed in the gas ratios at the surface ocean, and remnants of CDW were detected just below the zones of active convection. Evidence of glacial meltwater (through He and Ne) was found in TNBP near 600 m and in front of the Ross Ice Shelf. The former may be glacial meltwater outflow from the Nansen Ice Shelf, which may be a source of mid-depth DFe. Further analyses are still pending.

Air/ice/ocean interactions in TNBP

The coastal polynya observations of air-sea heat fluxes, waves and upper ocean ice formation reported here are focused primarily on the TNBP (Fig. 3b) given our longer occupation (over 12 days in early May), and the opportunity to observe several katabatic wind events exceeding 30 m s^{-1}.

Air-sea heat fluxes in TNBP

The highest heat fluxes observed in TNBP are sufficient to freeze sea ice at a rate of up to ~0.70 m day^{-1}, verifying that coastal polynyas can be effective 'ice factories'. Fluxes were observed during three 'fast transects' along the east-west axis of TNBP using rawinsonde balloon releases approximately every 2 hours. Radiosonde measurements during one of these transects in a strong katabatic wind event (with winds of up to 30 m s^{-1}) reveal the downwind effect on surface heat fluxes (Fig. 9). The transect started near the Nansen Ice Shelf in open water, swept clear of sea ice by high winds, and proceeded east into the advected area of newly formed sea ice, parallel to the Drygalski Ice Tongue (Fig. 3b). Heat fluxes computed from radiosonde observations by the integral method were in excess of 2000 W m^{-2} in the nearshore open water areas and decreased eastward into the ice-covered area. Around 50–60 km from the Ice Shelf (Fig. 9), heat fluxes increased again as we crossed a small open water polynya at the tip of the ice tongue. The heat fluxes then declined to below 200 W m^{-2} in the thicker pack ice outside of TNBP. The heat flux was comprised primarily of sensible and latent heat, with net longwave contributing ~10% to the total heat flux.

Frazil ice growth and SIP during katabatic wind events

Oceanographic observations during katabatic wind events are used to calculate frazil ice concentration and SIP rates (De Pace and others,2019). Eleven of the 17 CTD profiles acquired in the polynyas revealed bulges of warm, salty water extending downwards tens of meters from the surface (Fig. 10). As we would typically expect uniform profiles with vigorous convective heat loss, these observations suggest a release of latent heat and salt during unconsolidated frazil ice production in the upper ocean. A simplified salt budget is used to estimate in situ frazil ice concentrations between 332×10^{-3} and 24.4×10^{-3} kg m^{-3}, and measurements of turbulent kinetic energy dissipation (from SWIFT deployments in TNBP) suggest mixing lifetimes from 2 to 12 min. The corresponding

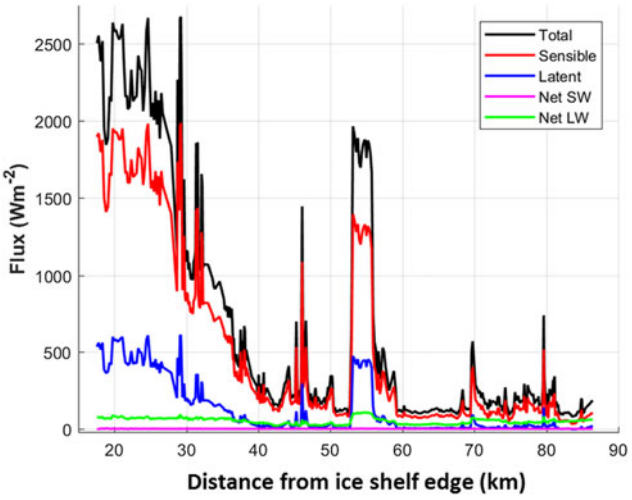

Fig. 9. Heat fluxes from a 'fast transect' at 75.2 S latitude in TNBP, starting ~10 km from the front of the Nansen Ice Shelf, and taken as the vessel traversed downwind from west to east. The sensible and latent heat fluxes shown here are estimates from a bulk method based on underway measurements of wind speed, temperature, humidity and surface temperature and roughness, with positive being upward towards the atmosphere. (Alternate heat flux calculations using the integral method based on changes in the downwind temperature and humidity produced similar values.)

median rate of SIP is 0.26 m day^{-1} and compares well with previous empirical and model estimates. Estimates of SIP from individual profiles are as high as 1.1 m day^{-1}.

Autumn-winter surface sensible heat fluxes over TNBP were also estimated using AWS data, atmospheric profiles acquired with an unmanned aerial vehicle and satellite-derived surface temperature data to compute fluxes over the period April–September for years 2003, 2005 and 2012–17 (the years with available data; Schick, 2018). The hourly average fluxes for the April to September period varied from ~450 W m^{-2} at the coast to ~165 W m^{-2} 30 km downwind of the coast. This heat loss from the ocean corresponds to seasonally-averaged SIP rates of 0.19 m day^{-1} near the coast and 0.07 m day^{-1} 30 km downwind of the coast, or a total of 30 m and 9 m respectively of sea-ice growth during the April–September period (Schick, 2018).

Waves in TNBP

The rapid formation of pancake ice observed in TNBP reflects the role of waves on ice growth. Pancake sea ice only forms in the presence of waves and has been previously observed to grow two to three times as fast as nilas (Doble and others, 2003). For PIPERS, it was critical to capture the evolution of waves in this dynamic environment. Surface waves and winds were measured during a katabatic wind event in TNBP using a SWIFT drifter (Fig. 11). We observed sustained, strong winds that are characteristic of katabatic wind events. Over the deployment, the drifter's distance from the coast (fetch) increased from 27 to 64 km, while the distance into the sea ice-covered area (b) simultaneously increased. As a result, wave heights decrease and the sea-ice growth slows down. These results demonstrate the strong relationship between waves and SIP in coastal polynyas (as well as in the MIZ). Further, results from such coupled in situ observations can be used to constrain and validate SIP rates in climate models with ice-wave coupling (e.g. Roach and others, 2019).

Summary

The PIPERS project conducted a comprehensive campaign in the seasonal sea-ice zone and coastal polynyas of the Ross Sea,

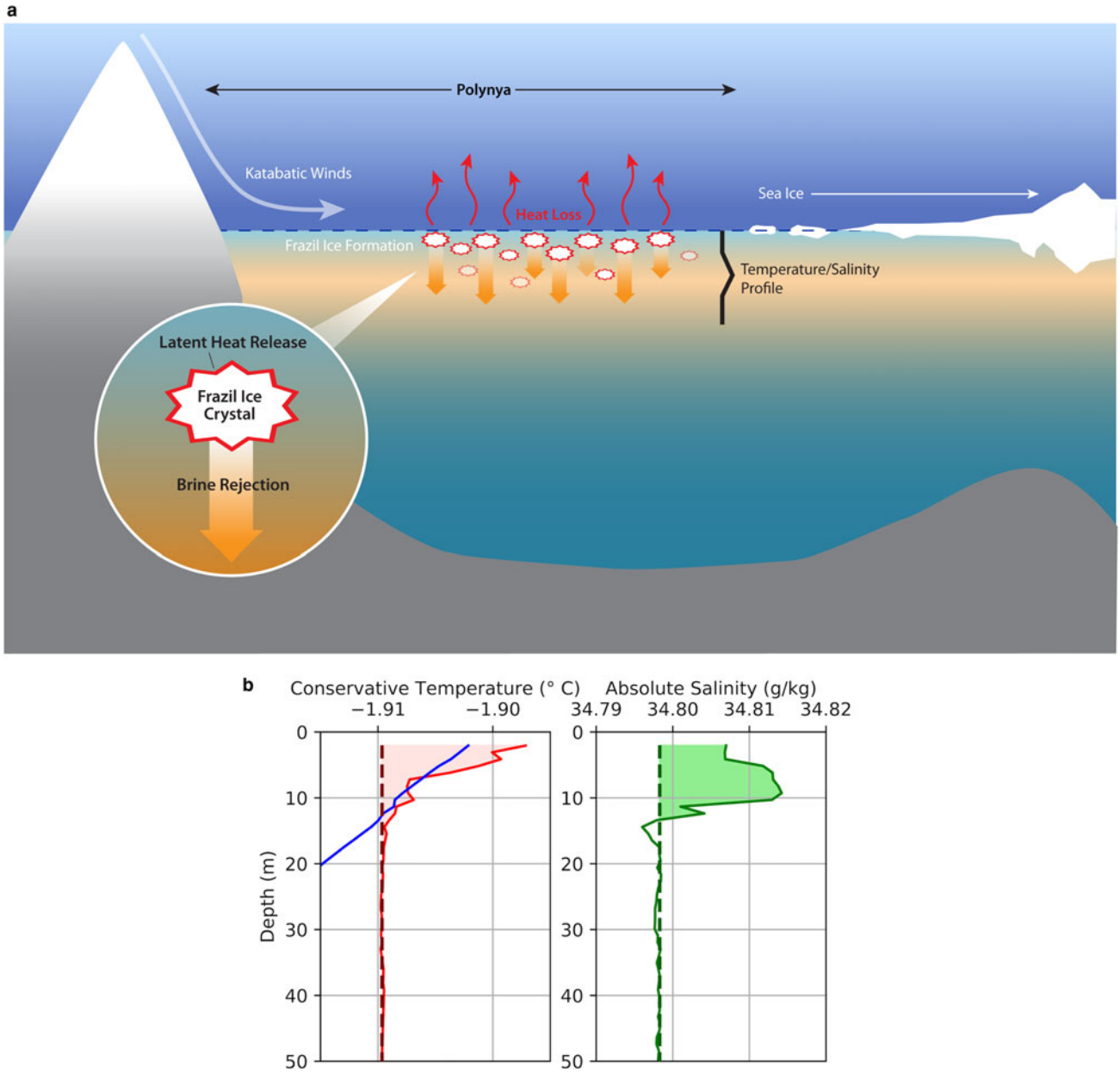

Fig. 10. (left) Schematic of frazil formation at depth during katabatic wind events. (right) Example temperature and salinity profiles from a CTD station in a katabatic wind event in TNBP. Shaded regions show the temperature and salinity anomaly compared to the baseline values (dotted line) where frazil ice is forming and releasing heat and salt. The blue line is the calculated freezing temperature (De Pace and others, 2019).

examining the coupled air-ice-ocean processes driving the autumn sea-ice advance and their impacts on biogeochemical processes. The regional atmospheric conditions in the Ross Sea in autumn are typically characterized by an interaction between (1) synoptic-scale (~2000 km) cyclones circling the Antarctic continent clockwise and (2) a variety of mesoscale (~200 km) features associated with the coastline, including intense katabatic wind events and mesoscale cyclones. The synoptic cyclones have the strongest effects in the more northerly and eastern parts of the Ross Sea. Toward the west, the cyclone-sheltering effect of the mountains of Victoria Land allows the mesoscale features to dominate the local forcing.

With respect to local forcing, PIPERS has increased our understanding of air/ice/ocean coupling under the different wind, wave and sea ice conditions observed in the coastal polynyas in particular. The comprehensive measurements of atmospheric structure and surface fluxes acquired during PIPERS in the TNBP specifically provided the first detailed in situ quantitative analyses of katabatic wind events, which are important to SIP and subsequent wind-driven advection of the newly formed sea ice. PIPERS fortuitously sampled 15 gale force wind events and one event at hurricane force in the TNBP. Although some mesoscale cyclones were observed in the Ross Sea during the cruise period, these were much weaker than the synoptic cyclones and katabatic winds, with the latter generating the strongest wind events ever observed.

The PIPERS observations were taken in the context of record low sea-ice extent, following an early ice edge retreat in spring-summer of 2016–17 and resulting in a nearly 2-month delay in autumn ice edge advance in 2017. The delayed ice-edge advance contributed to:

(1) Increased SIP and sea ice export in the coastal polynyas, with air-ocean heat fluxes of up to 2000 W m^{-2}, wind velocities of up to 30 m s^{-1}, significant wave heights of >2 m, frazil ice formation down to 10 m ocean depth, rapid formation of thin

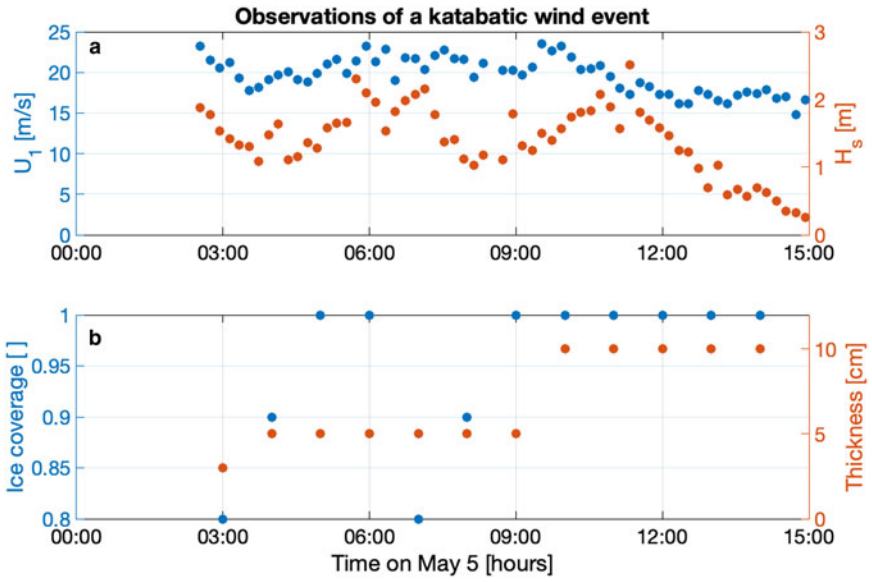

Fig. 11. (a) Wind speed (U_1, m s^{-1}) and wave height (H_s, m) observations from a SWIFT drifter deployed during katabatic wind events, and (b) coincident ASPeCt visual ice observations. Downwind distance from the coast was ~27 km at deployment, and 64 km at recovery.

pancake ice <0.2 m, and greater expanses of thin ice in the polynya outflows than was observed during the only other winter field campaign in the Ross Sea.

(2) Thinner snow and ice cover in the central pack with underway visual observations of level, undeformed pack ice showing modal values <0.40 m and snow cover <0.10 m.
(3) Lower sea ice Chl-*a* burdens and differences in the sea-ice sympagic communities.
(4) Delayed deepening of the winter mixed layer and a sustained ocean heat flux likely delaying ice thickening.
(5) A melting, anomalously southward ice edge persisting into winter.

Despite these impacts, spring airborne observations 5–6 months following the ship-based field campaign indicated that winter SIP over the continental shelf was likely not anomalous.

PIPERS acquired the first in situ coupled air/ice/ocean observations in an active coastal polynya (TNBP) in autumn. Repeated, strong katabatic wind events in TNBP drove the extreme loss of heat and copious ice production, high amplitude waves, and subsurface frazil ice formation at depths down to 10 m. Thin pancake ice was quickly removed from the formation area and thickened downstream by rafting. This rapid removal of ice, facilitated by both the intense katabatic wind events and a mobile pack exterior to the polynya, served to maintain a more active 'ice factory' than previously observed during the only other autumn-winter cruise to TNBP in 1998.

From air-ice-ocean data acquired in TNBP, three different methodologies were used to estimate SIP rates under different assumptions and over different space/timescales. The SIP rate estimates range from (1) 0.75 m day^{-1} (bulk/integrative calculation, based on hourly-to-daily timescales over ~90 km), (2) 0.26 to 1.1 m day^{-1} (instantaneous calculations, based on seconds-to-minutes timescales over ~km-scale distances), and (3) 0.19 to 0.07 m day^{-1} (from near the coast to 30 km downwind of the coast, based on seasonal averages over April to September). These different estimates reflect differences in space/timescales, assumptions and conditions, while also underscoring the challenges and complexities of measuring in situ SIP.

There is also the complex feedback between SIP and surface heat fluxes, as surface heat fluxes are highly dependent on whether there is ice cover and the type of ice present. The highest SIP rate by thermodynamic growth will be in areas of open water and will drop off strongly as the ice cover forms downwind, whereas the highest SIP rate by dynamic ice thickening will be downwind away from the coast, where new ice piles up. As highlighted by PIPERS, any future work on better resolving SIP rates will ideally involve multi-platforms and multi-methodologies under a range of forcing and surface conditions, if we hope to better understand the complex drivers of SIP.

Since 2016, record low sea-ice extents have occurred in the Ross Sea, in contrast to long-term sea-ice increases and record maxima observed 2013–2015. Given this context, future analysis of PIPERS data will be aimed towards understanding the drivers and consequences of the anomalous autumn ice advance on the ice/ocean/biogeochemical system. We have quantified SIP in the TNB coastal polynya, but identification of the air/ice/ocean interactions driving production and thickening of the pack ice along its northward trajectory to the ice edge is still in progress.

The late start of the autumn ice growth season resulted in a late start to winter ocean mixed layer deepening, Shelf Water production, and convective overturning particularly in the central Ross Sea. The warmer and shallower CDW on the outer continental shelf and northward (relative to climatological conditions) likely slowed sea ice thickening into winter-spring. Whether late winter SIP in the central/outer pack or continued high SIP and export in the coastal polynyas contributed to near-average sea-ice thickness observed by airborne campaigns in spring is still under investigation.

Data used in this paper are available at http://www.usap-dc.org/view/project/p0010032.

Acknowledgements. We are greatly indebted to the Antarctic Support Contractors who went above and beyond in supporting PIPERS extensive planning and logistics. We also thank the crew of the N. B. Palmer, for most of whom PIPERS was their first cruise on the N. B. Palmer and some not knowing they were going to Antarctica in the dark of night. (Tahiti was their end destination.) NSF supported PIPERS award numbers: ANT-1341717 (S.F. Ackley, UTSA); ANT-1341513 (E. Maksym, WHOI); ANT-1341606 (S. Stammerjohn and J. Cassano, U Colorado); ANT-1341725 (P. Guest, NPS). P. Sedwick was supported by NSF ANT-1543483. S.F. Ackley was also supported by NASA Grant 80NSSC19M0194 to the Center for Advanced Measurements in Extreme Environments at UTSA. S. Stammerjohn was also supported by the LTER Program under NFS award number ANT-0823101 (H. Ducklow, LDEO/Columbia University). Additional support was by the Belgian F.R.S-FNRS (project ISOGGAP and IODIne, contract T.0268.16 and J.0262.17, respectively). Bruno Delille is a research associate of the F.R.S.-FNRS. Terra-Sar-X quicklook imagery was coordinated by Kathrin Hoeppner at DLR, and Andy Archer (with the Antarctic Support Contractor) provided selected (cloud-free) MODIS scenes and daily maps of AMSR2 sea-ice concentration.

References

Adolphs U (1999) Roughness variability of sea ice and snow cover thickness profiles in the Ross, Amundsen, and Bellingshausen Seas. *Journal of Geophysical Research* **104**(C6), 13577–13591.

Arrigo KR, van Dijken GL and Bushinsky S (2008a) Primary production in the Southern Ocean, 1997–2006. *Journal of Geophysical Research: Oceans* **113**(C8), 6 pgs.

Arrigo KR, van Dijken G and Long M (2008b) Coastal Southern Ocean: a strong anthropogenic CO_2 sink. *Geophysical Research Letters* **35**(21), 6 pgs.

Comiso JC, Kwok R, Martin S and Gordon AL (2011) Variability and trends in sea ice extent and ice production in the Ross Sea. *Journal of Geophysical Research: Oceans* **116**(C4), 19 pgs. doi: 10.1029/2010JC006391.

Dai L, Xie H, Ackley S and Mestas-Nuñez A (2020) Ice production in Ross Ice Shelf Polynyas during 2017–2018 from Sentinel-1 SAR images. *Remote Sensing* **12**, 1484–1501.

de Lavergne C, Palter JB, Galbraith ED, Bernardello R and Marinov I (2014) Cessation of deep convection in the open Southern Ocean under anthropogenic climate change. *Nature Climate Change* **4**, 278–282. doi: 10.1038/nclimate2132.

De Pace L and 5 others (2019) Frazil ice growth and production during katabatic wind events in the Ross Sea, Antarctica. *The Cryosphere Discussions*, 15 pgs. doi: 10.5194/tc-2019-213.

Doble MJ, Coon MD and Wadhams P (2003) Pancake ice formation in the Weddell Sea. *Journal of Geophysical Research: Oceans* **108**(C7), 13 pgs. doi: 10.1029/2002JC001373.

Drucker R, Martin S and Kwok R (2011) Sea ice production and export from coastal Polynyas in the Weddell and Ross Seas. *Geophysical Research Letters* **38**(17), 4 pgs. doi: 10.1029/2011GL048668.

Garrison DL and 6 others (2005) Sea-ice microbial communities in the Ross Sea: autumn and summer biota. *Marine Ecology Progress Series* **300**, 39–52.

Gordon AL and 6 others (2004) Energetic plumes over the western Ross Sea continental slope. *Geophysical Research Letters* **31**(21), 4 pgs.

Hamme R and Emerson S (2004) The solubility of neon, nitrogen and argon in distilled water and seawater. *Deep Sea Research* **51**, 1517–1528. doi: 10.1016/j.dsr.2004.06.009.

Haumann FA, Gruber N, Münnich M, Frenger I and Kern S (2016) Sea-ice transport driving Southern Ocean salinity and its recent trends. *Nature* **537** (7618), 89–92. doi: 10.1038/nature19101.

Hobbs WR and 5 others (2016) A review of recent changes in Southern Ocean sea ice, their drivers and forcings. *Global and Planetary Change* **143**, 228–250. doi: 10.1016/j.gloplacha.2016.06.008.

Jackson K and 6 others (2013) A novel and low-cost sea ice mass balance buoy. *Journal of Atmospheric and Oceanic Technology* **30**(11), 2676–2688. doi: 10.1175/JTECH-D-13-00058.1.

Jacobs SS (2004) Bottom water production and its links with the thermohaline circulation. *Antarctic Science* **16**(4), 427–437. doi: 10.1017/S095410200400224X.

Jacobs SS and Giulivi CF (2010) Large multidecadal salinity trends near the Pacific-Antarctic continental margin, *Journal of Climate* **23**, 4508–4524. doi: 10.1175/2010JC13284.1.

Jeffries MO and Adolphs U (1997) Early winter ice and snow thickness distribution, ice structure and development of the western Ross Sea pack ice between the ice edge and the Ross Ice Shelf. *Antarctic Science* **9**(2), 188–200. doi: 10.1017/S0954102097000242.

Jeffries MO, Li S, Jaña RA, Krouse HR and Hurst-Cushing B (1998) Late winter first-year ice floe thickness variability, seawater flooding and snow ice formation in the Amundsen and ross seas. In Jeffries MO (ed.), *Antarctic Sea Ice: Physical Processes, Interactions and Variability.*

Jeffries MO, Morris K, Maksym T, Kozlenko N and Tin T (2001a). Autumn sea ice thickness, ridging and heat flux variability in and adjacent to Terra Nova Bay, Ross Sea, Antarctica. *Journal of Geophysical Research: Oceans* **106** (C3), 4437–4448. doi: 10.1029/1999JC000021.

Jeffries MO, Krouse HR, Hurst-Cushing B and Maksym T (2001b). Snow-ice accretion and snow-cover depletion on Antarctic first-year sea-ice floes. *Annals of Glaciology* **33**, 51–60. doi: 10.3189/172756401781818266.

Kern S and Spreen G (2015) Uncertainties in Antarctic sea-ice thickness retrieval from ICESat. *Annals of Glaciology* **56**(69), 107–119. doi: 10.3189/2015aog69a736.

Kohout A and 5 others (in press) Observations of exponential wave attenuation in Antarctic sea ice during the PIPERS campaign. *Annals of Glaciology* **81**(82).

Kwok R (2005) Ross Sea ice motion, area flux, and deformation. *Journal of Climate* **18**(18), 3759–3776. doi: 10.1175/JCLI3507.1.

Kwok R, Pang SS and Kacimi S (2017) Sea ice drift in the Southern Ocean: regional patterns, variability, and trends. *Elementa: Science of the Anthropocene* **5**, 32. doi: 10.1525/elementa.226.

Lecomte O and 5 others (2017) Vertical ocean heat redistribution sustaining sea-ice concentration trends in the Ross Sea. *Nature Communications* **8**(1), 1–8. doi: 10.1038/s41467-017-00347-4.

Liang JH and 5 others (2013) Parameterizing bubble-mediated air-sea gas exchange and its effect on ocean ventilation. *Global Biogeochemical Cycles* **27**, 894–905. doi: 10.1002/gbc.20080.

Loose B, McGillis WR, Perovich D, Zappa CJ and Schlosser P (2014). A parameter model of gas exchange for the seasonal sea ice zone. *Ocean Science* **10**, 17–28. doi: 10.5194/os-10-17-2014.

Marsay CM and 5 others (2014) Estimating the benthic efflux of dissolved iron on the Ross Sea continental shelf. *Geophysical Research Letters* **41** (21), 7576–7583.

McGillicuddy DJ Jr. and 6 others (2015) Iron supply and demand in an Antarctic shelf ecosystem. *Geophysical Research Letters* **42**(19), 8088–8097.

Meehl GA and 7 others (2019) Sustained ocean changes contributed to sudden Antarctic sea ice retreat in late 2016. *Nature Communications* **10**(1), 1–9. doi: 10.1038/s41467-018-07865-9.

Mei MJ, Maksym T, Weissling B and Singh H (2019) Estimating early-winter Antarctic sea ice thickness from deformed ice morphology. *The Cryosphere* **13**, 2915–2934. doi: 10.5194/tc-13-2915-2019.

Meredith MP and 7 others (2011) Synchronous intensification and warming of Antarctic Bottom Water outflow from the Weddell Gyre. *Geophysical Research Letters* **38**, L03603. doi: 10.1029/2010GL046265.

Nicholson D, Emerson S, Caillon N, Jouzel J and Hamme RC (2010) Constraining ventilation during deepwater formation using deep ocean measurements of the dissolved gas ratios 40Ar/36Ar, N2/Ar, and Kr/Ar. *Journal of Geophysical Research* **115**, C11015. doi: 10.1029/2010JC006152.

Orsi A and Wiederwohl C (2009) A recount of Ross Sea waters. *Deep-Sea Research II* **56**(13-14), 778–795. doi: 10.1016/j.dsr2.2008.10.033.

Parkinson CL and Cavalieri DJ (2012) Antarctic sea ice variability and trends, 1979–2010. *The Cryosphere* **6**(4), 871. doi: 10.5194/tc-6-871-2012.

Purich, A and England MH (2019) Tropical teleconnections to Antarctic sea ice during austral spring 2016 in coupled pacemaker experiments. *Geophysical Research Letters* **46**, 6848–6858. doi: 10.1029/2019GL082671.

Roach LA, Bitz CM, Horvat C and Dean SM (2019) Advances in modelling interactions between sea ice and ocean surface waves. *Journal of Advances in Modeling Earth Systems* **11**, 15 pgs. doi: 10.1029/ 2019MS001836.

Russo A and 5 others (2011) Climatology and decadal variability of the Ross Sea shelf waters. *Advances in Oceanography and Limnology* **2**(1), 55–77. doi: 10.1080/19475721.2011.575179.

Schick K (2018) *Influence of Weather and Surface Variability on Sensible Heat Fluxes in Terra Nova Bay, Antarctica* (Master thesis), Dept of Atm. Sciences, University of Colorado Boulder, CO, USA, pp. 29.

Schlosser E, Haumann FA and Raphael MN (2018). Atmospheric influences on the anomalous 2016 Antarctic sea ice decay. *The Cryosphere* **12**(3), 1103–1119. doi: 10.3929/ethz-b-000256143.

Sedwick PN, DiTullio GR and Mackey DJ (2000) Iron and manganese in the Ross Sea, Antarctica: seasonal iron limitation in Antarctic shelf waters. *Journal of Geophysical Research: Oceans* **105**(C5), 11321–11336.

Smith WO Jr., Sedwick PN, Arrigo KR, Ainley DG and Orsi AH (2012) The Ross Sea in a sea of change. *Oceanography* **25**(3), 90–103.

Smith M and Thomson J (2016) Scaling observations of surface waves in the Beaufort Sea. *Elementa: Science of the Anthropocene* **4**, 000097. doi: 10.12952/journal.elementa.000097.

Stammerjohn S, Massom R, Rind D and Martinson D (2012) Regions of rapid sea ice change: an inter-hemispheric seasonal comparison. *Geophysical Research Letters* **39**, L06501. doi: 10.1029/2012GL050874.

Stuecker MF, Bitz CM and Armour KC (2017). Conditions leading to the unprecedented low Antarctic sea ice extent during the 2016 austral spring season. *Geophysical Research Letters* **44**(17), 9008–9019. doi: 10.1002/2017GL07469.

Tagliabue A and Arrigo KR (2005) Iron in the Ross Sea: 1. Impact on CO_2 fluxes via variation in phytoplankton functional group and non-Redfield stoichiometry. *Journal of Geophysical Research: Oceans* **110**(C3), 15 pgs.

Tagliabue A and Arrigo KR (2016) Decadal trends in air-sea CO_2 exchange in the Ross Sea (Antarctica). *Geophysical Research Letters* **43**(10), 5271–5278.

Tamura T, Ohshima K and Nihashi S (2008) Mapping of sea ice production for Antarctic coastal polynyas. *Geophysical Research Letters* **35**(7), 5 pgs. doi: 10.1029/2007GL032903.

Tian L and 7 others (submitted) Sea ice freeboard and thickness in the Ross Sea from airborne altimetry (IcePod 2016–2017) and comparison with IceBridge 2013 and ICESat 2003–2008. *Remote Sensing*.

Tin T and Jeffries MO (2001) Sea-ice thickness and roughness in the Ross Sea, Antarctica. *Annals of Glaciology* **33**(1), 187–193. doi: 10.3189/172756401781818770.

Tin T and Jeffries MO (2003) Morphology of deformed first-year sea ice features in the Southern Ocean. *Cold Regions Science and Technology* **36**, 141–163. doi: 10.1016/s0165-232x(03)00008-9.

Tison JL, Delille B and Papadimitriou S (2017) *Sea Ice* (D. Thomas, ed.), pp. 433–471, ISBN 978-1-118-77838-8, Wiley-Blackwell

Tison JL and others (submitted) Physical and biological properties of early winter Antarctic sea ice in the Ross sea, *Annals of Glaciology*.

Turner J and 8 others (2009) Non-annular atmospheric circulation change induced by stratospheric ozone depletion and its role in the recent increase of Antarctic sea ice extent. *Geophysical Research Letters* **36**, L08502. doi: 10.1029/2009GL037524.

Turner J and 6 others (2017) Unprecedented springtime retreat of Antarctic sea ice in 2016. *Geophysical Research Letters* **44**, 6868–6875. doi: 10.1002/2017GL073656.

Turner J and Comiso J (2017) Solve Antarctic's sea-ice puzzle. *Nature News* **547**(7663), 275. doi: 10.1038/547019a.

Wanninkhof R (1992) Relationship between wind-speed and gas-exchange over the Ocean. *Journal of Geophysical Research: Oceans* **97**, 7373–7382. doi: 10.1029/92JC00188.

Williams G and 6 others (2015) Thick and deformed Antarctic sea ice mapped with autonomous underwater vehicles. *Nature Geoscience* **8**, 61–67. doi: 10.1038/ngeo2299.

Worby AP and 5 others (2008) Thickness distribution of Antarctic sea ice. *Journal of Geophysical Research: Oceans*, **113**(C5), 14 pgs. doi: 10.1029/2007JC004254.

Worby AP, Massom RA, Allison I, Lytle VI and Heil P (1998) East Antarctic sea ice: a review of its structure, properties, and drift. In Jeffries MO (ed.), *Antarctic Sea Ice: Physical Processes, Interactions and Variability*. Antarctic Research Series, vol. **74**. Washington DC: American Geophysical Union, pp. 41–67.